Science Advances
AAAS

Supplementary Materials for

Reprogrammable soft actuation and shape-shifting via tensile jamming

Bilige Yang, Robert Baines, Dylan Shah, Sreekalyan Patiballa, Eugene Thomas, Madhusudhan Venkadesan, Rebecca Kramer-Bottiglio*

*Corresponding author. Email: rebecca.kramer@yale.edu

Published 1 October 2021, *Sci. Adv.* **7**, eabh2073 (2021)
DOI: 10.1126/sciadv.abh2073

The PDF file includes:

Other Supplementary Material for this manuscript includes the following:

Note S1. Jamming fiber optimization and additional characterization

We conducted pull-to failure tensile tests (20 mm/min using an Instron 3345 fitted with a 50 N load cell) on individual segmented elasticity fibrils (SEFs) to shed light on the behavior of jamming fibers containing that type of SEF. Six types of SEF, containing differing volume fractions of polyester γ), were studied: 0%, 60% type A, 60% type B, 70% type A, 70% type B, and 100%. Note that 0% and 100% were selected as control specimens—0% is pure elastomer; 100% is pure polyester thread. A force versus displacement plot of the tests (Figure S3 A) reveals that the 0% SEFs were the least stiff (initial stiffness of 0.0012 N/mm). Increasing the volume fraction of polyester caused an increase in stiffness, peaking at pure polyester thread (initial stiffness of 0.47 N/mm).

Average elongation at failure was calculated from the force-displacement curves (Figure S3 B). There is a monotonically increasing trend in elongations at failure. Starting at around 23 mm for 100%, elongation rises to 130 mm for 70% of both types, to 160 mm for 60% of both types, and then 400 mm for 0%. SEFs of the same polyester volume fraction exhibited similar elongations at failure, regardless of whether there were type A or type B. This result implies that jamming fibers constituted of equal amounts type A and type B SEF should have relatively homogeneous stiffness properties along their length.

With an understanding of the mechanics of a single SEF, the fundamental unit that composes jamming fibers, we moved on to test the fibers themselves. To explore the design space for jamming fibers, we conducted unidirectional tensile tests on combinations of fiber parameters. In particular, we chose three vacuum pressures (-10 kPa, -20 kPa, and -40 kPa), four different numbers of SEFs (N = 4, 6, 8, 10), and two ratios of polyester (60% and 70%)—yielding a representative, though not comprehensive, range of designs. Each fiber used in the tensile tests was 120 mm long.

A set of tensile tests entailed a pull to 12 mm—what we deem normal operational range for the jamming fibers. 10% strain represents a factor of safety from performance degradation. We chose to stop the test at 10% strain because it was empirically determined that after 20% strain, the performance of a fiber was markedly degraded. The mean jammed stiffness of each combination is reported in Figure S4 A-B in 3D space to visualize the various parameter contributions to stiffness (in N/mm). The mean was also extracted and placed into Table S1, for ease of reference to specific values.

In addition, Figure S4 C-D gives the ratio of jammed to unjammed stiffnesses. We chose to proceed with the 70% N8 for subsequent testing and demonstrations because it exhibited the highest stiffness differential between jammed and unjammed states (aside from the 70% N10), and also demonstrated more repeatability than the 70% N10 specimens (perhaps due to the lower probability that SEFs would shift).

We performed pull-to-failure tests on several specimens of the selected type (70% N8) to study the maximum elongation and force of the type of fiber at different pressures (Figure S5). Expectantly, as the absolute value of pressure increased, the maximum load sustained by the fiber increased. From this test, we learned that fiber failure modes are characterized by three

Table S1: Table of stiffness values at varying pressures and polyester compositions

		Pressure, P (kPa)			
		0	-10	-20	-40
γ = 60%	N4	0.0145	0.0332	0.0577	0.0987
	N6	0.022	0.089	0.1054	0.1387
	N8	0.035	0.248	0.302	0.387
	N10	0.046	0.3	0.46	0.514
γ = 70%	N4	0.0226	0.20	0.2915	0.369
	N6	0.034	0.2287	0.4122	0.5879
	N8	0.035	0.27	0.568	0.783
	N10	0.047	0.32	0.61	0.846

stages. The first is slip of the SEFs relative to one another, which caused subtle drops in force over a longer duration. The second is incremental individual SEF failure inside the fiber. Incremental failure can be seen in the frequent "stair-step" drops in force toward the end of each curve. Notably, the lower the pressure, the more consistently and strongly a specimen was able re-accumulate force after a drop in force caused by internal SEFs failing. For example, the -40 kPa and -20 kPa curves exhibit sharp drops (it was observed at these moments individual SEFs were failing), followed by steep rises in force. On the other hand, the 0 kPa specimen had only meager gains in force once it experienced a drop. The third stage of fiber failure occurs when most of the individual SEFs have failed. At this point, the elastomer sleeve supports the majority of the load. It tended to fail in the gauge length, causing a final steep drop in force.

To evaluate the selected jamming fiber's behavior over a number of uses, two cyclic tensile tests were carried out at 60 mm/min displacement rates. Each cyclic test had max extension of 8 mm. In the first test, a fiber was jammed and subjected to 1000 cycles (Figure 2B). This test simulated cases where a fiber would be jammed for a long duration to coerce a single actuator trajectory multiple times. Some hysteresis occurred until about 50 cycles. After 50 cycles, the rate of hysteresis decreased, and began to plateau around 900 cycles. By cycle 1000, the force sustained by the jamming fiber only dropped from 5.1 N to 3.6 N (29% relaxation)—a testament to the long lifetime of the jamming fiber.

In the second cyclic test, we intermittently unjammed and jammed three fibers for 100 cycles, tracking how the force at each iteration changed (Figure 2C). This test mimicked real use cases for reconfigurable trajectories, where a given fiber might be jammed or unjammed, depending on the desired deformation. During the test, the maximum force at each cycle fluctuated, likely due to internal SEF shifting upon each unjam-jam cycle. In fact, the average force rises slightly over time. We attribute the rise to SEF re-alignment. As the sample is strained and subsequently released over and over, SEFs can "settle in" to favorable spots of overlap.

Additionally, we performed tension tests at 20 mm/min to quantify the effect of suddenly

transitioning from an jammed state to a unjammed state, and vice-versa. The tests sought to replicate a robotic application where changes to actuator trajectory occur mid-inflation. Three trials on different specimens, corresponding to different jammed pressures, were conducted (Figure S6 A-B).

From these jamming transition tests, we observed that the extent of pre-strain does not significantly influence the resultant force experienced by the fiber. In fact, there is less than 5% difference in maximum force sustained by any of the pressure cases between a and b. However, pre-strain does make the silicone material stiffer due to non-linearity of the elastomeric material, and explains the slightly higher final force in the case with pre-strain (Figure S6 A). As the pre-strain strain approaches the overlap percent of the SEFs, we suspect the peak force would be very different (*i.e.* the overlap regions will have decreased in area, yet the SEFs will be much stiffer due to non-linearity).

Lastly, we conducted 3-point bending tests on tensile jamming fibers to assess the change in bending modulus between the jammed and unjammed states. We tested three specimens in both jammed and unjammed states, and at 0 and 90-degree rotations, recording force and displacement (Instron 3345 fitted with a 10 N load cell). The supports on the two ends are separated by 4 cm. Displacement was applied in a quasi-static regime at 40 mm/min. Each specimen was subjected to -80 kPa when jammed. A linear fit of the force displacement curves indicates that bending stiffness (slope of a fitted line) increases by approximately 2-fold when jammed compared to unjammed (Figure 2C-D). Furthermore, the slope and max forces seen for both rotations are within 5% of one another, attesting to the isotropy of the fiber in bending. Even though there is a 2-fold stiffness increase from the unjammed to jammed state, we remark that the magnitude of the forces are still very small relative to the bending force exerted by soft robotic actuators. The benefit conferred by this low bending stiffness, namely negligible influence on system deformation when unjammed, are exemplified through demonstrations in Figures 3-6.

Note S2. Minimal model of jamming behavior

To understand the relationship between key design parameters and the jammed stiffness of the fibers, we constructed a minimal mechanical model. The purpose of the model is twofold. First, it is not tractable to manufacture tensile jamming fiber specimens to test all possible combinations of parameters in the design space, so an analytical model helps depict the general trend of stiffness change when different parameters are tuned. Second, the model can be used to estimate a suitable range of stiffnesses for a jamming fiber to accomplish a set of tasks, effectively providing a lightweight design tool.

Before the derivation, we state some preliminaries. We will refer to the individual segmented elastic fibril (SEF) simply as "fibril" for the rest of this section. The model only considers two fibrils and their shared interface for simplicity of analysis, but at the end of this section, we propose how the model could be generalized to include more fibrils. We assume that tensile forces are all in-line, due to the fact that the length of the fibril is much greater than its width or

height. Polyester and silicone are the two materials in the fibril. Since the Young's modulus of polyester is much larger than that of silicone, we further assume polyester to be inextensible.

In the unjammed state, we assume there is no contact between fibrils. Since polyester is treated as inextensible, the jamming fiber's stiffness in the tensile direction is a function of only the stiffness of silicone segments in each fibril (k_s) as well as in the surrounding membrane (k_m). In the jammed state, the fibrils are compressed together by uniform external pressure (ΔP). Thin interfaces form between overlaps of polyester-polyester, polyester-silicone, and polyester-membrane segments; shearing of these interfaces, when pulled, contributes additional stiffness terms (k_{pp}, k_{ps}, and k_{pm}, respectively). See the schematic in Figure S1 for a visual reference to quantities in the following derivation.

We define these various stiffness terms using material properties and dimensions of fibrils. The tensile stiffness of a single fibril (k_s) is modeled as linear:

$$k_s = \frac{EA_c}{L_{silicone}} = \frac{EA_c}{L(1-\gamma)}, \tag{3}$$

where E is the Young's modulus of silicone, L is the total length of the fibril, A_c is the cross section area of that fibril ($A_c = d^2$, assuming square shaped cross-section), and γ is the loading factor (length percentage of the fibril that is polyester). The tensile stiffness of a membrane (k_m) is likewise modeled as linear:

$$k_m = \frac{EA_m}{L} \tag{4}$$

where A_m is the cross sectional area of the silicone membrane.

We model the shear interfaces as Bingham plastics — a nonlinear spring that is linear with displacement until reaching a maximum constant force. The nonlinear behavior arises due to slip, which we will discuss later. Before slip, the slope of the linear region of these springs is simply the shear stiffness of the thin silicone interfaces: k_{pp}, k_{ps} and k_{pm}.

The pre-slip shear stiffness of the polyester-polyester interface reads as:

$$k_{pp} = \alpha \frac{GA_{pp}}{2t}, \tag{5}$$

where α is the effective contact ratio (a fitting parameter to account for imperfect contact), G is the shear modulus of silicone ($G = \frac{E}{2(1+\nu)}$ where ν is the Poisson ratio), A_{pp} is the area of shear between polyester and polyester ($A_{pp} = L_{pp}d$), and t is the thickness of the silicone under shear on one fibril. This thickness is a function of the applied pressure, since pressure will squeeze and flatten the silicone. We also represent thickness with a linear elastic model:

$$t(\Delta P) = t_0 - t_0 \frac{\Delta P}{E} \tag{6}$$

where t_0 is the initial thickness of the silicone interface. The shear stiffness of the polyester-silicone interface can be written as:

$$k_{ps} = \alpha \frac{GeA_{ps}}{t}, \tag{7}$$

where A_{ps} is the area between polyester and silicone spring ($A_{ps} = L_{ps}d$), t is the same as in equation 6, and e is a parameter to account for the fact that not all the area between polyester and the silicone spring is under shear ($e \leq 1$). Lastly, we define the shear stiffness of the polyester-membrane interface as:

$$k_{pm} = \alpha \frac{GA_{pm}}{t} \tag{8}$$

where A_{pm} is the area of shear between polyester and silicone membrane ($A_{pm} = L_{pm}d$).

We model collections of fibrils within the jamming fiber as springs in parallel, together with the external membrane. For the system of fibrils in the unjammed state, the only stiffness contributions are k_s and k_m. Thus, the unjammed stiffness of the system is:

$$k_u = \mathrm{N}k_s + k_m, \tag{9}$$

where N is the number of fibrils in the fiber. Note that neither the membrane dimensions nor its material composition are varied in the present paper, so k_m is a constant.

In the jammed state, we consider stiffness arising from all the interfaces as well as from the silicone spring and membrane (see Figure S1C, right). The total stiffness can be calculated through a combination of serial and parallel springs. For a two-fibril system:

$$k_{j,\mathrm{N}=2} = \frac{2k_{pm}(k_s+k_{ps})^2 + 2k_{pm}(k_s+k_{ps})k_{pp} + 2k_{pm}^2(k_s+k_{ps}) + k_{pm}^2k_{pp} + (k_s+k_{ps})^2k_{pp}}{2k_{pm}(k_s+k_{ps}) + 2k_{pm}k_{pp} + k_{pm}^2 + (k_s+k_{ps})^2 + 2(k_s+k_{ps})k_{pp}} + k_m \tag{10}$$

We can simplify this long expression based on the observation that k_{pm} and k_{pp} are much larger quantities than k_s and k_{ps} (for example, for one sample, $k_s = 2.28$ and $k_{ps} = 115.26$, while k_{pp} and k_{pm} are over 1000.) By eliminating terms with k_s and k_{ps} from equation 10, we have:

$$k_{j,\mathrm{N}=2} = \frac{k_{pm}^2k_{pp}}{2k_{pm} + k_{pm}^2} + k_m \tag{11}$$

To generalize to jamming fibers with $\mathrm{N} > 2$, we make the observation that, under single stacking, each additional fibril increases the total number of polyester-polyester interfaces by one. Since these interfaces are in parallel, we can simply multiply the k_{pp} term by the number of interfaces, $z = \mathrm{N} - 1$.

$$k_j = \frac{k_{pm}^2zk_{pp}}{2k_{pm}zk_{pp} + k_{pm}^2} + k_m \tag{12}$$

We can further simplify the expression by observing that k_{pm} and k_{pp} are approximately equal, as they are both shear stiffnesses of thin silicone: $k_{pm} \approx k_{pp} \approx k_{shear}$. Equation 12 thus simplifies to

$$k_j = \frac{zk_{shear}^3}{2zk_{shear}^2 + k_{shear}^2} = \frac{zk_{shear}^3}{(2z+1)k_{shear}^2} = \frac{z}{2z+1}k_{shear} \tag{13}$$

Plugging in some numbers for n and p into the expression above elucidates a general trend:

$$k_j|_{\mathrm{N}=2,z=1} = \frac{1}{3}k_{shear} \tag{14}$$

$$k_j|_{\mathrm{N}=3,z=2} = \frac{2}{5}k_{shear} \tag{15}$$

$$k_j|_{\mathrm{N}\to\infty,z\to\infty} = \frac{1}{2}k_{shear} \tag{16}$$

Namely, the model predicts higher stiffness with increased number of fibrils, which our experiments confirmed.

So far, we have considered stiffness of the jammed fiber before slip. Slip happens when the shear force in the interface exceeds the maximum static friction that can be sustained by the silicone interface between polyester threads in adjacent fibrils. The maximum force is defined as:

$$F_f^{max}(\Delta P) = \mu \Delta P A_{pp}, \tag{17}$$

where μ is the coefficient of static friction. After slip, the k_{pp} term vanishes in equation 10. The stiffness reduces to

$$k_{j,post-slip} = \frac{2k_{pm}(k_s + k_{ps})}{2(k_s + k_{ps}) + k_{pm}} + k_m \tag{18}$$

In the Table S2, we present all the parameters in the minimal jamming model along with their values used in generating the analytical predictions (dashed lines) in main text Figure 2A (tensile force versus displacement for 70% N8 samples). We used three fitting parameters: α, e, and μ. The values of the fitting parameters were determined via subjective perception of similarity between data and model.

Table S2: Table of parameters for minimal jamming model

Jamming Model Parameters			
Parameter	Description	Value	Source
E	Young's modulus of EcoFlex 30 silicone	82 kPa	data sheet
ν	Poisson's ratio	0.5	data sheet
L	Length of fibril	120 mm	measured
t_0	Initial thickness of silicone interface	1 mm	measured
A_c	Cross-sectional area of fibril	1 mm^2	measured
A_m	Cross-sectional area of membrane	25 mm^2	measured
A_{pp}	Area between polyester and polyester	48 mm^2	measured
A_{ps}	Area between polyester and silicone spring	48 mm^2	measured
A_{pm}	Area between polyester and membrane	72 mm^2	measured
α	Effective contact ratio	0.15	fitted
e	Shear area ratio	0.1	fitted
μ	Coefficient of friction	1.52	fitted

The root-mean-square deviation of the model prediction from the experimental results in Figure 2 A is 0.0296 N, 0.1331 N, 0.2346 N, and 0.2962 N, for the four pressure inputs (from 0 kPa to -40 kPa), respectively.

Overall, the presented minimal analytical model predicts a larger stiffness for higher number of fibrils, higher pressure, as well as a higher polyester content (higher tensile stiffness for fibrils), which we also observed in the experimental results (Figure S4A-B). For example, in the experimental results, increasing from N $= 4$ to N $= 10$ at P = 40 kPa and γ = 60$\%$ elevated the jammed stiffness by 420$\%$. With N $= 8$ at P = 40 kPa, increasing γ from 60% to 70% increased the stiffness by 52$\%$.

Note S3. Minimal model of cylindrical jamming fiber-reinforced actuators

Here we consider the equilibrium center line $\mathcal{D} \in \mathbb{R}^3$ attained by cylindrical thin-walled inflating elastomeric actuators radially outfitted in jamming fibers. We select a number of segments $i = 1...n$, an input pressure P for each segment, the number of SEFs on each segment $j = 1...q$, radial locations of jammed fibers for each segment $\theta_{i,j}$, and initial undeformed geometry (*i.e.* radius, R, wall thickness, T, length L).

We consider radially-constrained cylindrical pneumatic actuators outfitted in jamming fibers along their length such that input pressure P elicits only longitudinal stretch λ_1, curvature κ, if applicable, and negligible radial stretch λ_2. We assume that κ appears only in the kinematics, and therefore not as a coupled energetic contribution with stretching. The actuators have small thickness relative to their radii (*i.e.* $R > 10T$).

To predict the deformation of an inflating actuator, we first derive a hyperelastic constitutive model mapping P to λ_1. For the inflating actuator, $\mathbf{B} = \mathbf{F}\mathbf{F}^T$ is the left Cauchy-Green deformation tensor and $\mathbf{F}$ is the deformation gradient. Assuming the elastomeric material which it is made from is incompressible gives $det(\mathbf{F}) = \lambda_1\lambda_2\lambda_3 = 1 \implies \lambda_3 = \frac{1}{\lambda_1\lambda_2}$. The N-term strain energy density of a deformed elastomer according to Ogden is (*67*):

$$W = \sum_{p=1}^{N} \frac{\mu_p}{\alpha_p}(\lambda_1^{\alpha_p} + \lambda_2^{\alpha_p} + \lambda_3^{\alpha_p} - 3) \tag{19}$$

Here, μ_p and α_p are fitting constants. Evoking the assumption of incompressibility:

$$W = \sum_{p=1}^{N} \frac{\mu_p}{\alpha_p}(\lambda_1^{\alpha_p} + \lambda_2^{\alpha_p} + \frac{1}{\lambda_1^{\alpha_p}\lambda_2^{\alpha_p}} - 3) \tag{20}$$

The Cauchy stress tensor may be found from W by the following:

$$\sigma_{ij} = -\bar{p}\delta_{ij} + \mathbf{F}_{jk}\frac{\partial W}{\partial \mathbf{F}_{jk}} \tag{21}$$

where $\bar{p}$ is an undetermined hydrostatic pressure to be found using the boundary conditions, and δ_{ij} is the Kronecker delta. We consider pure homogeneous deformation associated with uniaxial tension which makes **F** diagonal. Thus the expression for Cauchy stress simplifies to:

$$\sigma_i = \bar{p} + \lambda_i \frac{\partial W}{\partial \lambda_i} \tag{22}$$

By substituting W into the expression above we get:

$$\sigma_i = \sum_{p=1}^{N} \mu_p \lambda_i^{\alpha_p} - \bar{p} \tag{23}$$

For uniaxial tension, σ_2 and $\sigma_3 = 0$, so:

$$\sigma_1 = \sum_{p=1}^{N} \mu_p \lambda_1^{\alpha_p} - \bar{p} \tag{24}$$

From the boundary conditions given above, we can solve for the unknown hydrostatic pressure as:

$$\bar{p} = \sum_{p=1}^{N} \mu_p \lambda_1^{-\frac{\alpha_p}{2}} \tag{25}$$

Finally, plugging $\bar{p}$ to the expression for σ_1 gives us:

$$\sigma_1 = \sum_{p=1}^{N} \mu_p (\lambda_1^{\alpha_p} - \lambda_1^{-\frac{\alpha_p}{2}}) \tag{26}$$

Modeling the cylinder as a thin-walled pressure vessel, by Laplace's law we have (*68*):

$$\sigma_1 = \frac{Pr}{2t} \tag{27}$$

Note, the capital variables R, T specify the undeformed configuration, while r, t denote the deformed configuration of the actuator. Yet $r = R$ due to the radially constraining fibers. Since volume is conserved in the incompressible material, $t = \frac{T}{\lambda_1}$. Plugging in eq. (26) to eq. (25) and re-arranging gives:

$$P = \frac{2T}{R} \sum_{p=1}^{N} \mu_p (\lambda_1^{\alpha_p - 1} - \lambda_1^{-\frac{\alpha_p}{2} - 1}) \tag{28}$$

Inflating in a quasi-static regime, we were able to fit equation (27) for $N = 2$ to experimental data of P versus λ_1 via a least-squares method in MATLAB. The adjusted R^2 value for the fit was 0.984. The two-term Ogden model parameters are tabulated in table S3.

Table S3: Table of parameters for Ogden model.

Ogden Model Parameters Fit	
Parameter	Value
α_1	1.915
α_2	3.019
μ_1	3.842
μ_2	-0.3533

Utilizing equation (27), a given input P may be mapped to λ_1. We assume jamming fibers, when jammed, are completely inextensible. Induced bending of the actuator is assumed to be of a constant κ. $\theta_{i,j}$ of the jamming fibers determines ϕ_i, the direction of curvature, of the ith segment. We consider three distinct cases for the direction of curvature based on empirical observations: 1) If only one fiber is jammed, we assume curvature will occur circumferentially aligned with the jammed fiber; 2) if multiple but not all fibers are jammed, we assume curvature will occur as the geometric midpoint about the circumference of the actuator between jammed fibers (for example, if there are jamming fibers on segment 1 at two locations $\theta_{1,1} = \pi/2$ and $\theta_{1,2} = \pi$, bending occurs at the angle $\phi_1 = 3\pi/4$); 3) if jammed fibers are directly opposite one another or all fibers are jammed, then no extension will occur. To find the value of κ, λ_1 is used, by projecting onto the plane of curvature and evoking the relation:

$$\kappa = \frac{\lambda_1 - 1}{r(\lambda_1 + 1)} \tag{29}$$

To account for n cylindrical segments placed in series to form continuum manipulators, we simply apply the P to λ_1 relationship to each individually. We account for relative positions of segments via homogeneous transformation matrices. Construction of possible $\mathcal{D}$ for arbitrary design parameters is thus achieved. Quantitatively, the analytical model tended to under-predict the extent of deformation in actual systems, suggesting that it is a conservative estimate of the actuator's capabilities. However, it captures deformations within a reasonable margin of error (Figure 4 C). We thus contend that the governing physics of the cylindrical actuator outfitted in jamming fibers can be encapsulated with the assumptions made in this minimal model.

Our minimal analytical model allows for simple prediction of how changing the relative radii of the actuator to jamming fiber would influence deformation. By equation 27, for a fixed input pressure, decreasing R will consequently decrease σ. The decrease in σ will correspond to a decrease in axial stretch (λ_1) given by a nonlinear relationship defined by the two-term Ogden hyperelastic model. The decrease in λ_1 correspondingly reduces the curvature defined in 29. In Figure S7, we show how κ changes as a function of λ_1, for a variety of fixed R.

Note S4. Minimal model of jamming membranes

In this section, we consider the possible shapes that can be elicited by inflating a planar, membrane-like surface with jamming fibers on either side. An approximate model of the system gives insight into the rapid, localized shape change that we are able to demonstrate. The membrane is approximated as a bilayer system with each layer having equal thickness. We leverage findings from non-Euclidian plates as well as incompatible elasticity theory (*69, 70*), and treat the 3D problem in a dimensionally-reduced fashion. Namely, the membrane is modeled as a 2D mid-plane surface. In differential geometry, 2D surfaces may be fully characterized by two tensors: a metric tensor, (the first fundamental form) **a**, which contains all information about lateral distances between points, and a curvature tensor, **b**, (the second fundamental form) which contains information about the local curvatures (*71*). An elastic sheet is characterized by two additional tensors: a natural metric $\bar{\mathbf{a}}$, and the natural curvature $\bar{\mathbf{b}}$. These tensors represent the lateral distances and curvatures that would make the sheet locally stress-free (*72*).

The constrained membrane system, when inflated, is hypothesized to deform so as to minimize the sum of its elastic bending and stretching energies. The total elastic energy of an incompatible non-Euclidean plate is given by (*72*):

$$U_{total} = \int [(1-v)tr((\mathbf{a}-\bar{\mathbf{a}})^2)+vtr^2(\mathbf{a}-\bar{\mathbf{a}})]\sqrt{|\bar{\mathbf{a}}|}]dA+\frac{h^2}{3}\int [(1-v)tr((\mathbf{b}-\bar{\mathbf{b}})^2)+vtr^2(\mathbf{b}-\bar{\mathbf{b}})]\sqrt{|\bar{\mathbf{a}}|}]dA \tag{30}$$

Here, v is the Poisson ratio (assumed at 0.5), and h is the thickness of the bilayer system. The first addend of the energy term corresponds to stretching energy and the second to bending energy. Expressions for the natural metric and curvature tensors read as:

$$\bar{\mathbf{a}} = \begin{bmatrix} \Lambda_{0,1}^2 & 0 \\ 0 & \Lambda_{0,2}^2 \end{bmatrix}, \bar{\mathbf{b}} = \begin{bmatrix} k_{0,1} & 0 \\ 0 & k_{0,2} \end{bmatrix}, \tag{31}$$

Here, $\Lambda_{0,i}$ and $k_{0,i}$ are mid-plane stretch and curvature of a fictional 1D bilayer beam cut from the 2D bilayer surface in principal direction i. A 1D beam cut from the surface can satisfy the deformation behaviors of individual layers of the bilayer when adhered together, while the 2D system cannot, since it is incompatible. Mid-plane stretch and curvature of the fictional beam can be computed analytically as (*74*):

$$\Lambda_0 = \frac{(\lambda_{tb}(\lambda_{tb}+mn(3+\lambda_{tb}+m(3+m+m^2n+3(1+m)\lambda_{tb}))))}{(m^4n^2+2m(2+m(3+2m))n\lambda_{tb}+\lambda_{tb}^2)} \tag{32}$$

$$k_0 = \frac{(6(\lambda_{tb}-1)m(1+m)^2n(m^4n^2+2m(2+m(3+2m))n\lambda_{tb}+\lambda_{tb}^2))}{(-h\lambda_{tb}(\lambda_{tb}+mn(3+\lambda_{tb}+m(3+m+m^2n+3(1+m)\lambda_{tb})))^2)} \tag{33}$$

where λ_{tb} is the stretch of the top layer relative to the bottom layer in a given principal direction, n is the ratio of moduli of top to bottom layer, and m is the ratio of thickness of top to bottom layer. In our case, m and $n = 1$ since the layers are made of the same material and have the same thicknesses.

The exact orientation of the jamming fibers on either side of the membrane surface will govern the way it deforms when inflated, and result in different equilibrium surfaces. We assume any fibers placed on the membrane act as a homogeneous composite and that the strain gradient across the surface is zero. We consider three distinct cases of fiber orientation: 1) One side with $90^\circ + 0^\circ$ and the other with 0° or 90° will elicit a cylindrical shape; 2) One side with $90^\circ + 0^\circ$ and the other unconstrained (isotropic growth) will elicit a hemispherical cap shape at lower stretch; 3) Sides with orthogonal activated jamming fibers will exhibit a saddle-like shape.

For case 1, bending is only along one axis, resulting in zero Gaussian curvature. Natural tensors $\bar{\mathbf{a}}$ and $\bar{\mathbf{b}}$ will have only one non-zero diagonal entry each. We thus reduce the problem further to a one-dimensional case in the principal direction of interest, analogous to the classical bimetallic thermostat of Timoshenko (*73*). Due to reduction to a 1D beam, relations (31) and (32) may be used to compute the resulting midsurface shape.

Cases 2 and 3 are a bit more complicated, since both stretching and bending energy terms compete to inform the equilibrium shape. For case 2, following the example presented in work by Pezzulla et al. (*74*), we can minimize the total energy, consisting of the sum of stretching and bending energies given by equation (29). Note that before the bifurcation regime exhibited by spherical caps wherein bending becomes energetically favorable over stretching, the natural metric does not diverge much from the metric (*74*). Thus we can assume $\mathbf{a} = \bar{\mathbf{a}}$. Natural tensor $\bar{\mathbf{b}}$ will have two equal non-zero diagonal entries. Generic entries of the second fundamental form read as

$$\mathbf{b} = \begin{bmatrix} L & M \\ M & N \end{bmatrix}, \tag{34}$$

and note that $M = 0, L = N$ due to the emergence of symmetric, hemispherical cap. Minimization of the energy (29) with respect to L gives analytic relation that can be solved for a single value of $\hat{L}$ as a function of the non-dimensionalized natural curvature $\hat{k_0}$:

$$\hat{L} + \gamma^4(\hat{L} - \hat{k_0}) = 0 \tag{35}$$

where the hats indicate non-dimensionalization of the term by $1/h$ and γ is a dimensionless, shape-dependent parameter (*74*).

Case 3 is tackled by similar energetic arguments as case 2. Natural tensors $\bar{\mathbf{a}}$ and $\bar{\mathbf{b}}$ will have only two non-zero diagonal entries of equal magnitudes, while the natural curvature tensor has entries with opposite-signed values. Fundamental forms of an energetically equivalent monolayer for case 3 are presented eloquently as (*64*):

$$\mathbf{a} = \frac{1+\lambda^2}{2}\begin{bmatrix} 1 & 0 \\ 0 & 1 \end{bmatrix}, \quad \mathbf{b} = \frac{3(\lambda-1)(\lambda+1)}{4h}\begin{bmatrix} -1 & 0 \\ 0 & 1 \end{bmatrix} \tag{36}$$

Here, λ is the midplane stretch of the bilayer system.

Using the first and second fundamental forms, we can find the principal curvatures of a surface by solving (*71*):

$$det(\mathbf{b} - k_i\mathbf{a}) = 0, \quad i = 1, 2 \tag{37}$$

The Gaussian curvature and mean curvature are then, respectively,

$$K = k_1 k_2, \quad H = \frac{1}{2}(k_1 + k_2) \tag{38}$$

Since we are assuming homogeneous fiber distribution in a given principle direction, we are unable to capture the local buckling of material between each fiber and thereby much of the topographical nuance of the physical systems. Furthermore, this simplified model does not account for variations in in-plane strain across the surface. Despite the mechanical simplifications, qualitatively, predictions from this minimal model of jamming-fiber clad membrane midplanes matches the corresponding experiments (Figure 6). Qualitative agreement suggests we have identified some of the governing mechanics at play in the actual system.

Note S5. Finite element analysis (FEA) simulations

To validate the experiments with a higher degree of fidelity than analytical methods, we performed finite element analysis (FEA) simulations in a commercial software package (ABAQUS). Nonlinear quasi-static analyses considering gravity were performed.

The cylindrical actuators of Figures 4 and 5 were modeled as elastomeric chambers wound with radially constraining polyester fibers and axially-constraining jamming fibers. The dimensions of the individual cylindrical actuator units matched those of the experiment, with inner radius 11.3 mm, outer radius 12.5 mm, and length 120 mm. One end of the actuator is completely fixed, and a pressure load of 10 kPa, matching experimental conditions, is applied to the actuator's inner surface. The elastomeric chamber of each was modeled as an incompressible Mooney-Rivlin (C_{01} = 0.0104 Mpa, C_{10} = 0.0214 Mpa for Elastosil 50 (*75*)) hyperelastic material and implemented as 10-node quadratic tetrahedron elements, with hybrid formulation (C3D10H). The radially constraining fibers ($E = 31.1$ GPa, $\nu = 0.36$) and axially oriented jamming fibers were modeled as linear elastic materials, and implemented as 2-node linear beam elements with a hybrid formulation (B31H). The stiffness values used for fully jammed, partially jammed, and unjammed fibers were computed from tensile tests, and are tabulated in Table S1.

Nonlinear quasi-static analysis was performed in ABAQUS/Explicit to simulate the shape deformation of the circular membrane of Figure 6. For these simulations, a pressure load of 10 kPa was applied radially to the membrane's inner surface. The shape-changing membrane was modeled as an enclosed circular shell. Jamming fibers were approximated as shell patches atop the circular membrane. The jamming patches were constrained to the surface of the circular membrane using a *TIE constraint. The membrane was modeled as an incompressible Mooney-Rivlin hyperelastic material, and jamming patches were modeled as a linear elastic material, analogous to the cylindrical actuator simulations. 4-node doubly curved shell elements (S4R) were used for circular membrane and jamming fibers. The jamming fibers' width was 5 mm, and the fibers were separated by a distance of 25 mm center-to-center.

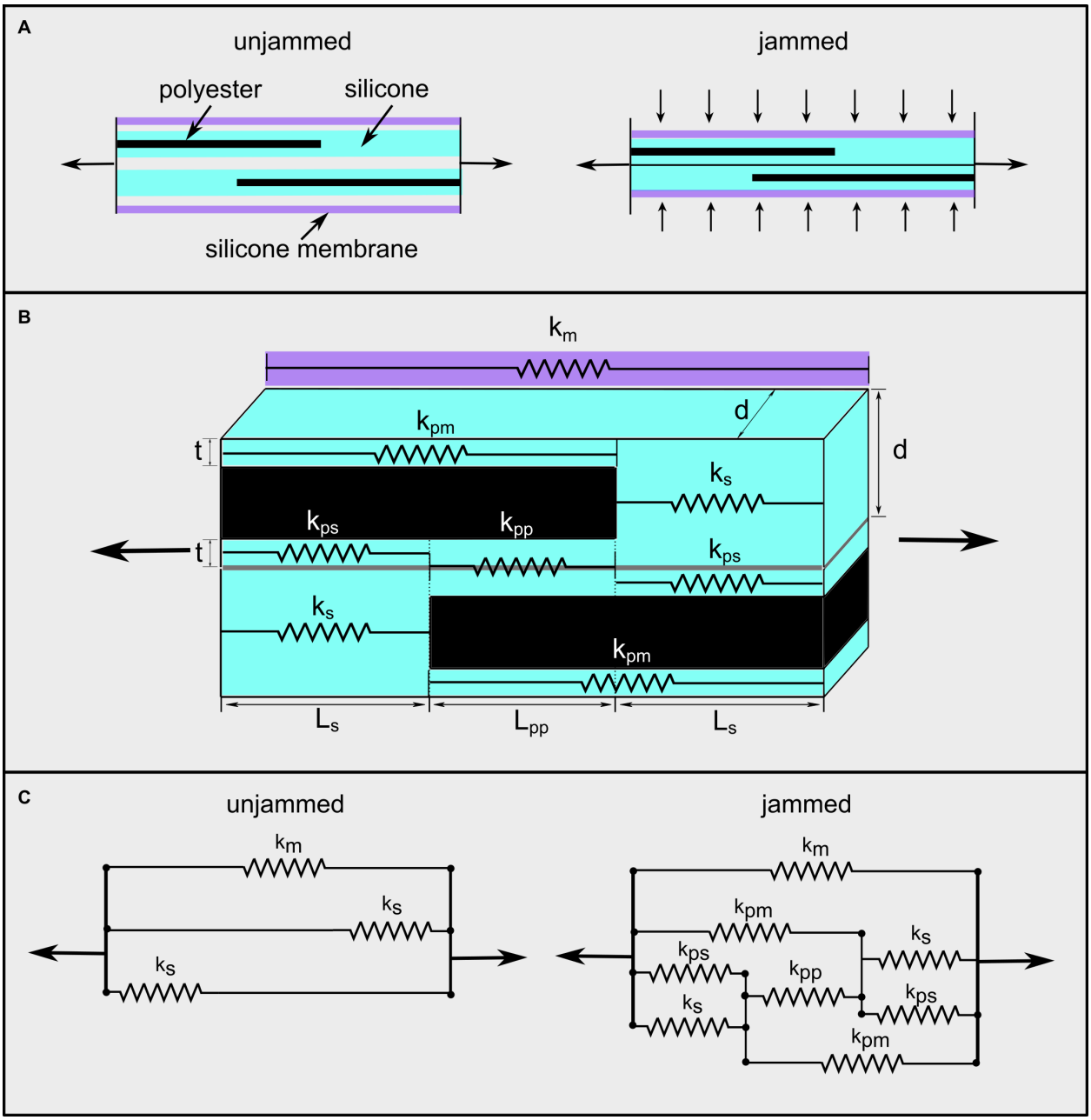

Figure S1: **Schematic of analytical model of jamming.** **(A)** schematic showing the fiber behavior in the unjammed and jammed cases. Only two fibrils are shown for simplicity. **(B)** A detailed drawing of the geometry of two jammed fibrils and their interface. Equivalent spring constants of different sections are shown. **(C)** Spring model of the unjammed and jammed cases of a two-fibril system.

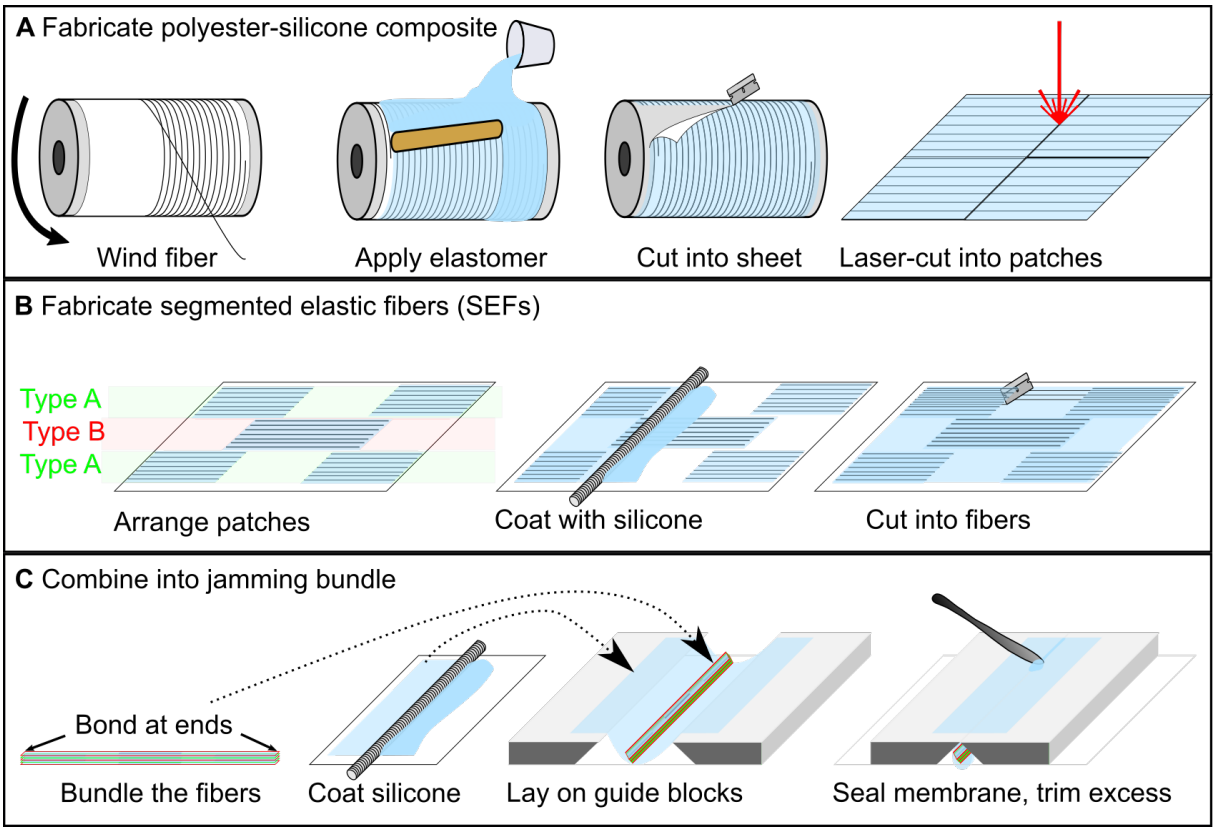

Figure S2: **Fabrication of jamming fibers.** (**A**) Fabricate a polyester-silicone composite laminae introduced in previous work (*22*). Wind polyester around a drum at 1 mm spacing, and apply an even coating of uncured silicone (DragonSkin 10 Medium, Smooth-On). Let the silicone cure while the drum is rotating to get even thickness. Then, cut the laminate material off from the drum, and laser-cut the laminae into smaller patches (size depending on the length of polyester thread we need in the SEF). (**B**) Fabricate SEFs. Arrange the patches on a flat surface according to the the type of SEF, coat with silicone (EcoFlex 50, Smooth-On), let cure, and cut into fibrils of width 1 mm (and height about 0.6 mm). (**C**) Combine constituent fibrils into jamming fiber. Stack alternating type A and type B SEFs, align them at both ends, and bond them with Silpoxy to make an unsealed fiber. Then, coat uncured silicone onto a flat surface for the silicone membrane. Allow that silicone to cure, put the membrane on two slide-able guide blocks, put the unsealed fiber inside, close the guide blocks, seal membrane with Silpoxy, and attach tubing.

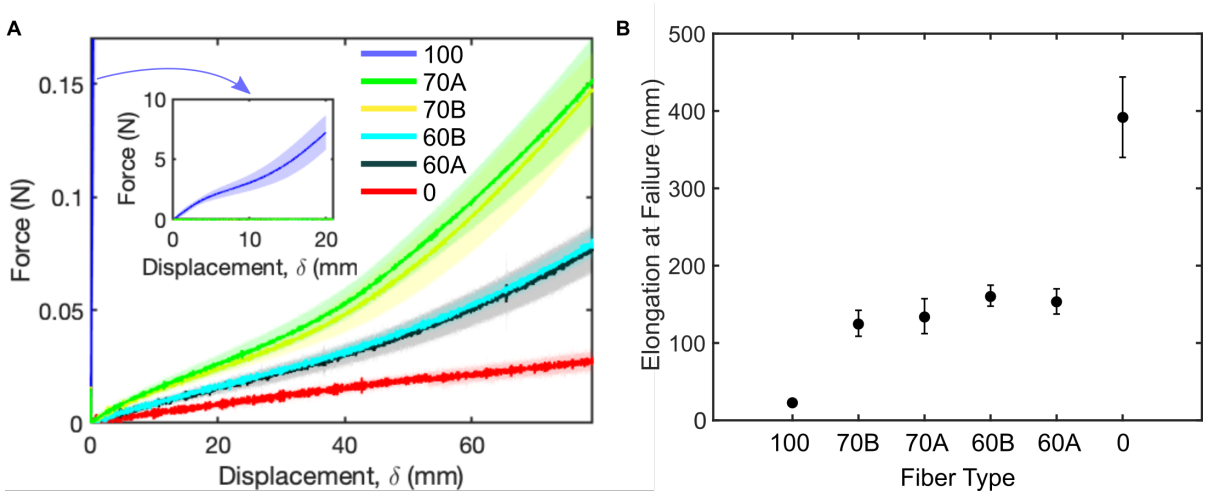

Figure S3: **Behavior of single SEF.** (**A**) Mean curves with standard deviation clouds for uniaxial tension tests of individual fibrils. Inset shows the small displacement regime to more clearly visualize the mechanical behavior of polyester fibers. (**B**) Elongation at failure of the various SEF specimens. Bars indicate a standard deviation above and below the mean of five samples.

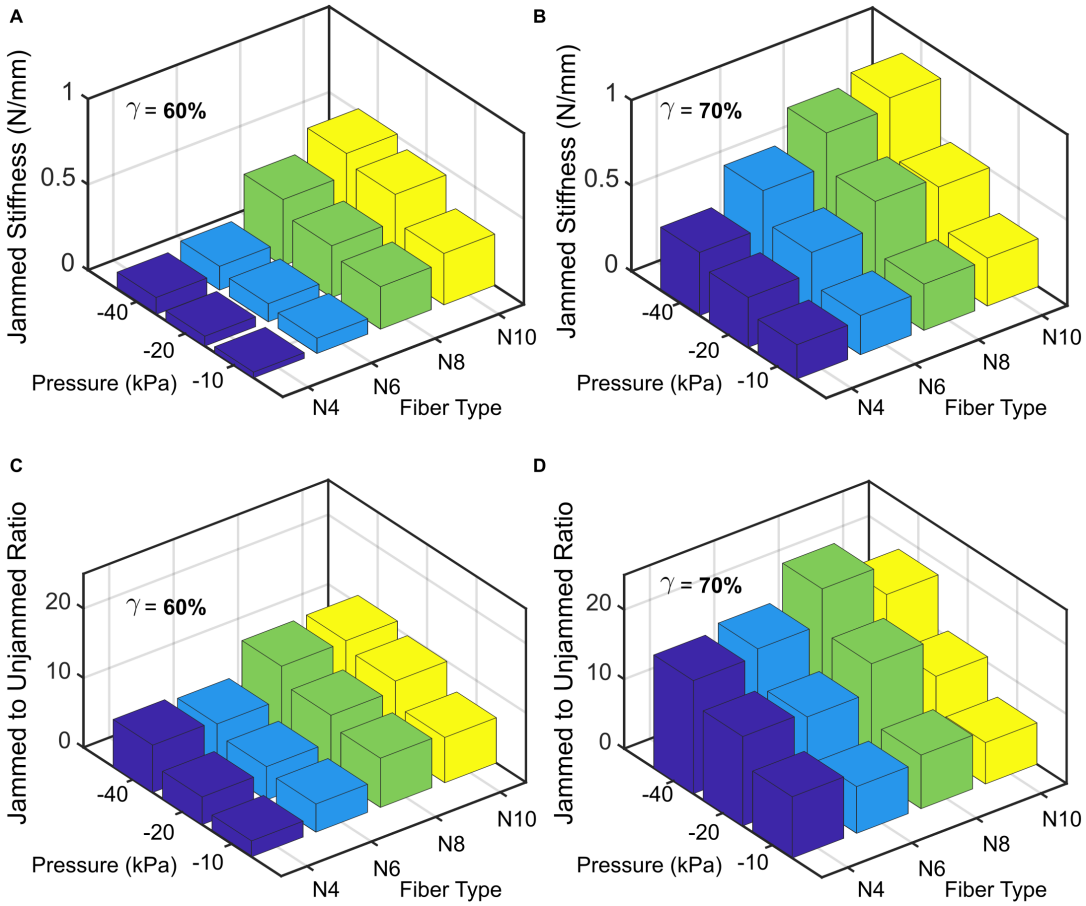

Figure S4: **Behavior of jammed fibers.** (**A**) Jammed fiber stiffness at various design parameters, holding $\gamma = 60\%$. (**B**) The same parameter sweep holding holding $\gamma = 70\%$. Reported values for A and B are mean values of three samples at each design point. (**C**-**D**) Ratio of jammed to unjammed stiffness values, holding $\gamma = 60\%$ or $\gamma = 70\%$.

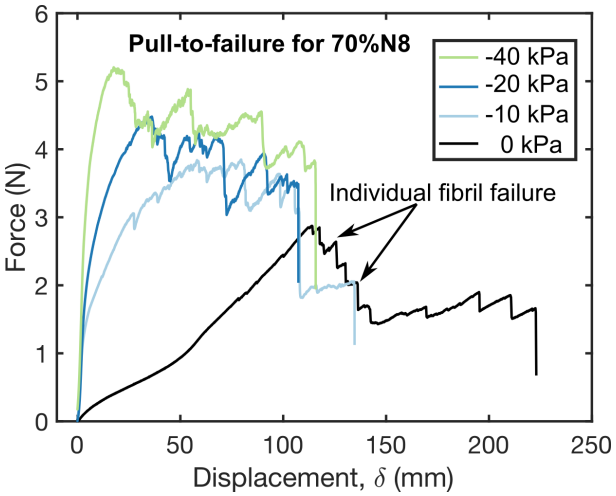

Figure S5: Pull-to-failure test on 70% N8 fiber at various pressures.

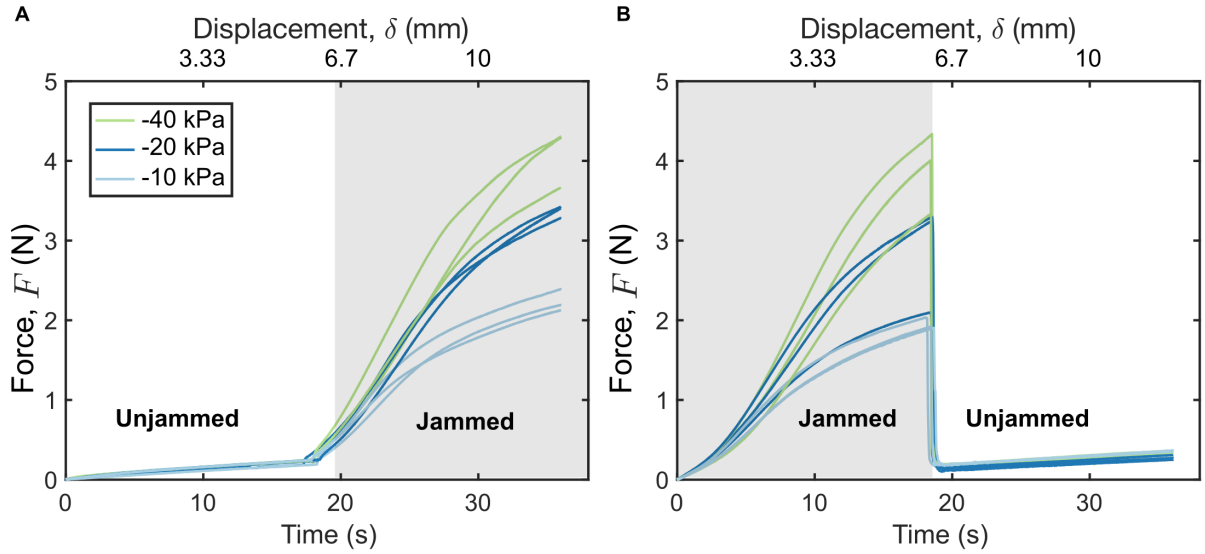

Figure S6: **Dynamic jamming.** (**A**) Dynamic transition from unjammed to jammed at displacement of 6 mm, at various pressures. Data from three samples at each pressure are plotted. (**B**) Dynamic transition from jammed to unjammed. Data from three samples at each pressure are plotted.

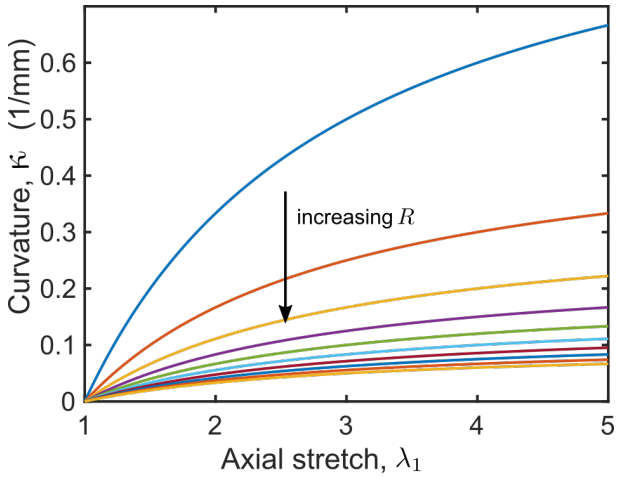

Figure S7: **Analytical model: curvature versus axial stretch** A direct consequence of our curvature model for the jamming-fiber clad cylindrical actuators is a monotonically increasing relation between axial stretch λ_1 and curvature κ. Here we show curves for a variety of different actuator radii spanning R =1 to 10mm in 1mm increments.

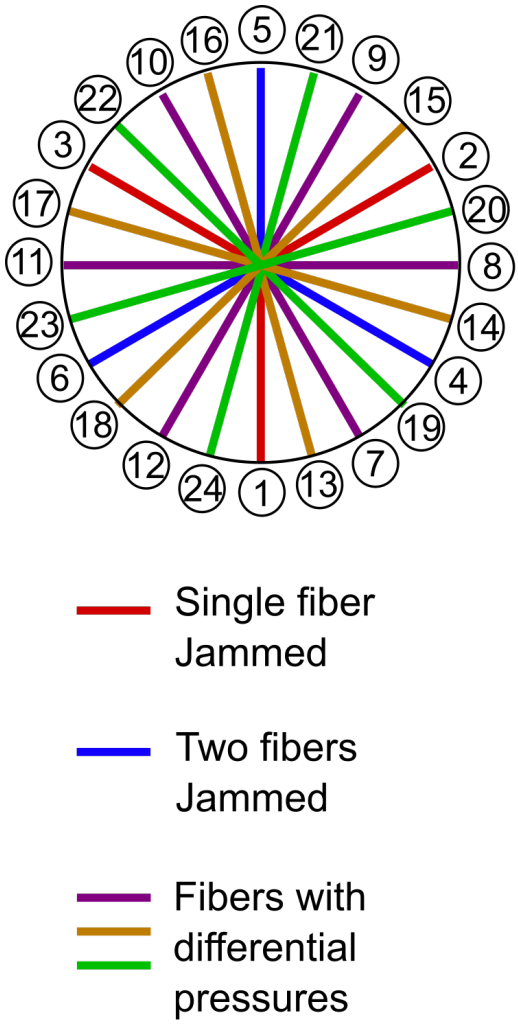

Configuration	$(x,y,z)_{final}$ (mm)
1	(0.04, -71.06, -6.77)
2	(61.52, 35.56, -6.77)
3	(-61.56, 35.46, -6.77)
4	(59.84, -34.37, -13.15)
5	(-0.15, 69.01, -13.15)
6	(-59.68, -34.64, -13.15
7	(32.68, -53.88, -3.96)
8	(63.01, 1.36, -3.96)
9	(30.32, 55.24, -3.96)
10	(-32.68, 53.88, -3.96)
11	(-63.01, -1.36, -3.96)
12	(-30.32, -55.24, -3.96)
13	(15.20, -63.98, -3.95)
14	(63.01, -18.83, -3.95)
15	(47.81, 45.15, -3.95)
16	(-15.20, 63.98, -3.95)
17	(-63.01, 18.83, -3.95)
18	(-47.81, -45.15, -3.95)
19	(45.15, -47.81, -3.95)
20	(63.98,15.2,-3.95)
21	(18.83, 63.01, -3.95)
22	(-45.15, 47.81, -3.95)
23	(-63.98, -15.2, -3.95)
24	(-18.83, -63.01, -3.95)

Figure S8: **Single actuator going in 24 directions in FEA.** The coordinates are the final x-y-z locations of the end effector.

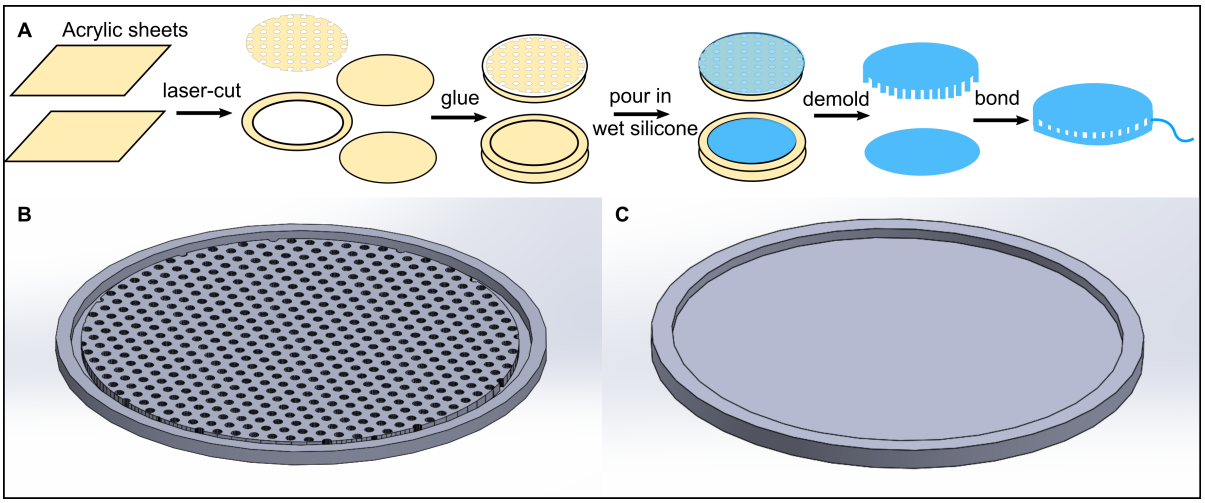

Figure S9: **Fabrication of planar actuator** (**A**) Acrylic sheets were laser-cut and then glued together with adhesives into molds. Wet silicone was poured into acrylic molds and cured at room temperature. De-molded silicone layers were adhered using uncured silicone. Pneumatic tubing was inserted and sealed with silicone glue. (**B**) CAD drawing of the top surface mold for pneumatic bladder. (**C**) CAD drawing of the bottom surface mold for pneumatic bladder.

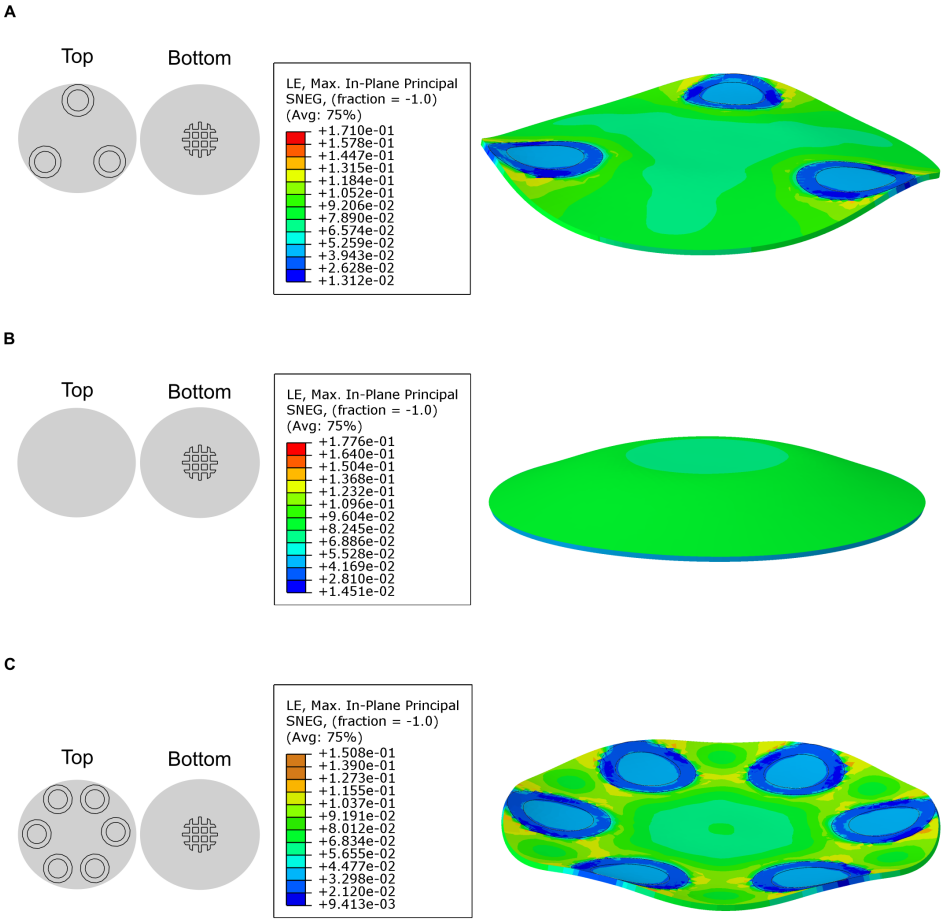

Figure S10: **Complex shapes generated by a large membrane with jamming fibers.** A single simulated large-scale membrane with patterned jamming fibers (six circles on top and orthogonal localized fibers on bottom) was able to morph to multiple distinct and complex topologies. (**A**) A topology with arches around three sides, saddles around three corners, and a central bowl, formed by activating orthogonal fibers on the bottom and fibers patterned in a three of the circles on top. (**B**) A shallow dome, formed by jamming just the bottom orthogonal fibers. (**C**) An even more complex topology formed when jamming all fibers.

Movie S1: **Variable stiffness jamming fibers.** Jamming fibers are easily stretchable at atmospheric pressure; under vacuum, the fibers increase in tensile stiffness and can sustain significant load.

Movie S2: **Omnidirectional actuator.** We applied tensile jamming fibers evenly spaced around an extending pneumatic actuator. By selectively jamming different fibers prior to actuating the central chamber, the actuator can bend in multiple directions.

Movie S3: **Three-fingered gripper.** We created a gripper made from three omnidirectional actuators and a flat palm. The gripper is capable of pinching, outward-hooking, and twisting grasping modes.

Movie S4: **Two-segment continuum arm.** Multiple actuators can be placed in series to make a continuum robot arm with distinct, dynamic trajectories.

Movie S5: **Shape-shifting membrane.** Several fibers were patterned on both sides of an expanding membrane. Jamming subsets of the fibers and actuating the membrane elicited surfaces with zero, positive, and negative Gauss curvatures.

REFERENCES AND NOTES

1. D. Shah, B. Yang, S. Kriegman, M. Levin, J. Bongard, R. Kramer-Bottiglio, Shape changing robots: Bioinspiration, simulation, and physical realization. *Adv. Mater.* **33**, 2002882 (2020).

2. G. Sumbre, G. Fiorito, T. Flash, B. Hochner, Motor control of flexible octopus arms. *Nature* **433**, 595–596 (2005).

3. G. Sumbre, G. Fiorito, T. Flash, B. Hochner, Octopuses use a human-like strategy to control precise point-to-point arm movements. *Curr. Biol.* **16**, 767–772 (2006).

4. J. Brackenbury, Caterpillar kinematics. *Nature* **390**, 453 (1997).

5. J. Brackenbury, Fast locomotion in caterpillars, *J. Insect Physiol.* **45**, 525–533 (1999).

6. S. Tadokoro, S. Yamagami, M. Ozawa, T. Kimura, T. Takamori, K. Oguro, Soft micromanipulation device with multiple degrees of freedom consisting of high polymer gel actuators, in *Proceedings of the Technical Digest. IEEE International MEMS 99 Conference. Twelfth IEEE International Conference on Micro Electro Mechanical Systems (Cat. No. 99CH36291)* (IEEE, 1999), pp. 37–42.

7. E. Hawkes, B. An, N. M. Benbernou, H. Tanaka, S. Kim, E. D. Demaine, D. Rus, R. J. Wood, Programmable matter by folding. *Proc. Natl. Acad. Sci. U.S.A.* **107**, 12441–12445 (2010).

8. C. T. Nguyen, H. Phung, T. D. Nguyen, H. Jung, H. R. Choi, Multiple-degrees-of-freedom dielectric elastomer actuators for soft printable hexapod robot. *Sens. Actuator A Phys.* **267**, 505–516 (2017).

9. J. Zhou, J. Yi, X. Chen, Z. Liu, Z. Wang, Bcl-13: A 13-dof soft robotic hand for dexterous grasping and in-hand manipulation. *IEEE Robot. Autom. Lett.* **3**, 3379–3386 (2018).

10. D. S. Shah, M. C. Yuen, L. G. Tilton, E. J. Yang, R. Kramer-Bottiglio, Morphing robots using robotic skins that sculpt clay. *IEEE Robot. Autom. Lett.* **4**, 2204–2211 (2019).

11. K. Suzumori, S. Iikura, H. Tanaka, Applying a flexible microactuator to robotic mechanisms. *IEEE Control Syst.* **12**, 21 (1992).

12. B. Shih, D. Drotman, C. Christianson, Z. Huo, R. White, H. I. Christensen, M. T. Tolley, Custom soft robotic gripper sensor skins for haptic object visualization, in *Proceedings of the 2017 IEEE/RSJ International Conference on Intelligent Robots and Systems (IROS)* (IEEE, 2017), pp. 494–501.

13. M. A. Robertson, J. Paik, New soft robots really suck: Vacuum-powered systems empower diverse capabilities. *Sci. Robot.* **2**, eaan6357 (2017).

14. R. V. Martinez, J. L. Branch, C. R. Fish, L. Jin, R. F. Shepherd, R. M. Nunes, Z. Suo, G. M. Whitesides, Robotic tentacles with three-dimensional mobility based on flexible elastomers. *Adv. Mater.* **25**, 205–212 (2013).

15. R. Xie, M. Su, Y. Zhang, Y. Guan, 3D-PSA: A 3d pneumatic soft actuator with extending and omnidirectional bending motion, in *Proceedings of the 2018 IEEE International Conference on Robotics and Biomimetics (ROBIO)* (IEEE, 2018), pp. 618–623.

16. Y. Elsayed, A. Vincensi, C. Lekakou, T. Geng, C. Saaj, T. Ranzani, M. Cianchetti, A. Menciassi, Finite element analysis and design optimization of a pneumatically actuating silicone module for robotic surgery applications. *Soft Robot.* **1**, 255–262 (2014).

17. M. Runciman, A. Darzi, G. P. Mylonas, Soft robotics in minimally invasive surgery. *Soft Robot.* **6**, 423–443 (2019).

18. K. C. Galloway, P. Polygerinos, C. J. Walsh, R. J. Wood, Mechanically programmable bend radius for fiber-reinforced soft actuators, in *Proceedings of the 2013 16th International Conference on Advanced Robotics (ICAR)* (IEEE, 2013), pp. 1–6.

19. Y. Sun, Y. S. Song, J. Paik, Characterization of silicone rubber based soft pneumatic actuators, in *Proceedings of the 2013 IEEE/RSJ International Conference on Intelligent Robots and Systems* (IEEE, 2013), pp. 4446–4453.

20. R. Deimel, O. Brock, A novel type of compliant and underactuated robotic hand for dexterous grasping. *Int. J. Rob. Res.* **35**, 161–185 (2016).

21. F. Connolly, C. J. Walsh, K. Bertoldi, Automatic design of fiber-reinforced soft actuators for trajectory matching. *Proc. Natl. Acad. Sci. U.S.A.* **114**, 51–56 (2017).

22. S. Y. Kim, R. Baines, J. Booth, N. Vasios, K. Bertoldi, R. Kramer-Bottiglio, Reconfigurable soft body trajectories using unidirectionally stretchable composite laminae. *Nat. Commun.* **10**, 3464 (2019).

23. T. L. Buckner, M. C. Yuen, S. Y. Kim, R. Kramer-Bottiglio, Enhanced variable stiffness and variable stretchability enabled by phase-changing particulate additives. *Adv. Funct. Mater.* **29**, 1903368 (2019).

24. A. Tonazzini, S. Mintchev, B. Schubert, B. Mazzolai, J. Shintake, D. Floreano, Variable stiffness fiber with self-healing capability. *Adv. Mater.* **28**, 10142–10148 (2016).

25. A. Firouzeh, M. Salerno, J. Paik, Soft pneumatic actuator with adjustable stiffness layers for multi-dof actuation, in *Proceedings of the 2015 IEEE/RSJ International Conference on Intelligent Robots and Systems (IROS)* (IEEE, 2015), pp. 1117–1124.

26. J. Santoso, E. H. Skorina, M. Salerno, S. de Rivaz, J. Paik, C. D. Onal, Single chamber multiple degree-of-freedom soft pneumatic actuator enabled by adjustable stiffness layers. *Smart Mater. Struct.* **28**, 035012 (2019).

27. L. Wang, Y. Yang, Y. Chen, C. Majidi, F. Iida, E. Askounis, Q. Pei, Controllable and reversible tuning of material rigidity for robot applications. *Mater. Today* **21**, 563–576 (2018).

28. S. Rich, S.-H. Jang, Y.-L. Park, C. Majidi, Liquid metal-conductive thermoplastic elastomer integration for low-voltage stiffness tuning. *Adv. Mater. Technol.* **2**, 1700179 (2017).

29. M. A. McEvoy, N. Correll, Thermoplastic variable stiffness composites with embedded, networked sensing, actuation, and control. *J. Compos. Mater.* **49**, 1799–1808 (2015).

30. S. Diller, C. Majidi, S. H. Collins, A lightweight, low-power electroadhesive clutch and spring for exoskeleton actuation, in *Proceedings of the 2016 IEEE International Conference on Robotics and Automation (ICRA)* (IEEE, 2016), pp. 682–689.

31. R. Hinchet, H. Shea, High force density textile electrostatic clutch. *Adv. Mater. Technol.* **5**, 1900895 (2020).

32. E. Steltz, A. Mozeika, J. Rembisz, N. Corson, H. Jaeger, Jamming as an enabling technology for soft robotics, in *Electroactive Polymer Actuators and Devices (EAPAD) 2010* (International Society for Optics and Photonics, 2010), vol. 7642, p. 764225.

33. M. Manti, V. Cacucciolo, M. Cianchetti, Stiffening in soft robotics: A review of the state of the art. *IEEE Robot. Autom. Mag.* **23**, 93–106 (2016).

34. S. G. Fitzgerald, G. W. Delaney, D. Howard, A review of jamming actuation in soft robotics, in *Actuators* (Multidisciplinary Digital Publishing Institute, 2020), vol. 9, p. 104.

35. B. Aktaş, R. D. Howe, Tunable anisotropic stiffness with square fiber jamming, in *Proceedings of the 2020 3rd IEEE International Conference on Soft Robotics (RoboSoft)* (IEEE, 2020), pp. 879–884.

36. E. Brown, N. Rodenberg, J. Amend, A. Mozeika, E. Steltz, M. R. Zakin, H. Lipson, H. M. Jaeger, Universal robotic gripper based on the jamming of granular material. *Proc. Natl. Acad. Sci. U.S.A.* **107**, 18809–18814 (2010).

37. N. G. Cheng, M. B. Lobovsky, S. J. Keating, A. M. Setapen, K. I. Gero, A. E. Hosoi, K. D. Iagnemma, Design and analysis of a robust, low-cost, highly articulated manipulator enabled by jamming of granular media, in *Proceedings of the 2012 IEEE International Conference on Robotics and Automation* (IEEE, 2012), pp. 4328–4333.

38. M. Cianchetti, T. Ranzani, G. Gerboni, T. Nanayakkara, K. Althoefer, P. Dasgupta, A. Menciassi, Soft robotics technologies to address shortcomings in today's minimally invasive surgery: The STIFF-FLOP approach. *Soft Robot.* **1**, 122–131 (2014).

39. A. Jiang, T. Ranzani, G. Gerboni, L. Lekstutyte, K. Althoefer, P. Dasgupta, T. Nanayakkara, Robotic granular jamming: Does the membrane matter? *Soft Robot.* **1**, 192–201 (2014).

40. T. Ranzani, G. Gerboni, M. Cianchetti, A. Menciassi, A bioinspired soft manipulator for minimally invasive surgery. *Bioinspir. Biomim.* **10**, 035008 (2015).

41. J. Ou, L. Yao, D. Tauber, J. Steimle, R. Niiyama, H. Ishii, jamsheets: Thin interfaces with tunable stiffness enabled by layer jamming, in *Proceedings of the 8th International Conference on Tangible, Embedded and Embodied Interaction* (Association for Computing Machinery, 2014), pp. 65–72.

42. Y. S. Narang, J. J. Vlassak, R. D. Howe, Mechanically versatile soft machines through laminar jamming. *Adv. Funct. Mater.* **28**, 1707136 (2018).

43. N. Vasios, Y. Narang, B. Aktaş, R. Howe, K. Bertoldi, Numerical analysis of periodic laminar and fibrous media undergoing a jamming transition. *Eur. J. Mech. - A/Solids* **75**, 322–329 (2019).

44. M. Brancadoro, M. Manti, S. Tognarelli, M. Cianchetti, Preliminary experimental study on variable stiffness structures based on fiber jamming for soft robots, in *Proceedings of the 2018 IEEE International Conference on Soft Robotics (RoboSoft)* (IEEE, 2018), pp. 258–263.

45. M. Brancadoro, M. Manti, F. Grani, S. Tognarelli, A. Menciassi, M. Cianchetti, Toward a variable stiffness surgical manipulator based on fiber jamming transition. *Front. Robot. AI* **6**, 12 (2019).

46. M. Brancadoro, M. Manti, S. Tognarelli, M. Cianchetti, Fiber jamming transition as a stiffening mechanism for soft robotics. *Soft Robot.* **7**, 663–674 (2020).

47. S. Jadhav, M. R. A. Majit, B. Shih, J. P. Schulze, M. T. Tolley, Variable stiffness devices using fiber jamming for application in soft robotics and wearable haptics. *Soft Robot.* (2021).

48. Y.-J. Kim, S. Cheng, S. Kim, K. Iagnemma, A novel layer jamming mechanism with tunable stiffness capability for minimally invasive surgery. *IEEE Trans. Robot.* **29**, 1031–1042 (2013.

49. Y. Yang, Y. Zhang, Z. Kan, J. Zeng, M. Y. Wang, Hybrid jamming for bioinspired soft robotic fingers. *Soft Robot.* **7**, 292–308 (2020).

50. X. Wang, L. Wu, B. Fang, X. Xu, H. Huang, F. Sun, Layer jamming-based soft robotic hand with variable stiffness for compliant and effective grasping. *Cognit. Comput. Syst.* **2**, 44–49 (2020).

51. I. Choi, N. Corson, L. Peiros, E. W. Hawkes, S. Keller, S. Follmer, A soft, controllable, high force density linear brake utilizing layer jamming. *IEEE Robot. Autom. Lett.* **3**, 450–457 (2017).

52. W. H. Choi, S. Kim, D. Lee, D. Shin, Soft, multi-dof, variable stiffness mechanism using layer jamming for wearable robots. *IEEE Robot. Autom. Lett.* **4**, 2539–2546 (2019).

53. D. S. Shah, E. J. Yang, M. C. Yuen, E. C. Huang, R. Kramer-Bottiglio, Jamming skins that control system rigidity from the surface. *Adv. Funct. Mater.* **31**, 2006915 (2020).

54. G. Chapman, The hydrostatic skeleton in the invertebrates. *Biol. Rev.* **33**, 338–371 (1958).

55. W. M. Kier, K. K. Smith, Tongues, tentacles and trunks: The biomechanics of movement in muscular-hydrostats. *Zool. J. Linn. Soc.* **83**, 307–324 (1985).

56. S. Kriegman, S. Walker, D. Shah, M. Levin, R. Kramer-Bottiglio, J. Bongard, Automated shapeshifting for function recovery in damaged robots. arXiv:1905.09264 [cs.RO] (22 May 2019).

57. M. Ishida, D. Drotman, B. Shih, M. Hermes, M. Luhar, M. T. Tolley, Morphing structure for changing hydrodynamic characteristics of a soft underwater walking robot. *IEEE Robot. Autom. Lett.* **4**, 4163–4169 (2019).

58. D. S. Shah, J. P. Powers, L. G. Tilton, S. Kriegman, J. Bongard, R. Kramer-Bottiglio, A soft robot that adapts to environments through shape change. *Nat. Mach. Intell.* **3**, 51–59 (2021).

59. D.-Y. Lee, S.-R. Kim, J.-S. Kim, J.-J. Park, K.-J. Cho, Origami wheel transformer: A variable-diameter wheel drive robot using an origami structure. *Soft Robot.* **4**, 163–180 (2017).

60. H.-T. Lin, G. G. Leisk, B. Trimmer, Goqbot: A caterpillar-inspired soft-bodied rolling robot. *Bioinspir. Biomim.* **6**, 026007 (2011).

61. K. Liu, F. Hacker, C. Daraio, Robotic surfaces with reversible, spatiotemporal control for shape morphing and object manipulation. *Sci. Robot.* **6**, eabf5116 (2021).

62. E. Reyssat, L. Mahadevan, Hygromorphs: From pine cones to biomimetic bilayers. *J. R. Soc. Interface* **6**, 951–957 (2009).

63. S. Armon, E. Efrati, R. Kupferman, E. Sharon, Geometry and mechanics in the opening of chiral seed pods. *Science* **333**, 1726–1730 (2011).

64. W. M. van Rees, E. Vouga, L. Mahadevan, Growth patterns for shape-shifting elastic bilayers. *Proc. Natl. Acad. Sci. U.S.A.* **114**, 11597–11602 (2017).

65. A. S. Gladman, E. A. Matsumoto, R. G. Nuzzo, L. Mahadevan, J. A. Lewis, Biomimetic 4d printing. *Nat. Mater.* **15**, 413–418 (2016).

66. J. W. Boley, W. M. van Rees, C. Lissandrello, M. N. Horenstein, R. L. Truby, A. Kotikian, J. A. Lewis, L. Mahadevan, Shape-shifting structured lattices via multimaterial 4d printing. *Proc. Natl. Acad. Sci. U.S.A.* **116**, 20856–20862 (2019).

67. A. G. Holzapfel, *Nonlinear Solid Mechanics II* (John Wiley & Sons, Inc., 2000).

68. R. R. Craig, *Mechanics of Materials* (John Wiley & Sons, Inc., 2011).

69. E. Efrati, E. Sharon, R. Kupferman, Buckling transition and boundary layer in non-Euclidean plates. *Phys. Rev. E* **80**, 016602 (2009).

70. E. Efrati, E. Sharon, R. Kupferman, Elastic theory of unconstrained non-euclidean plates. *J. Mech. Phys. Solids* **57**, 762–775 (2009).

71. D. J. Struik, *Lectures on Classical Differential Geometry* (Courier Corporation, 1961).

72. Y. Klein, E. Efrati, E. Sharon, Shaping of elastic sheets by prescription of non-Euclidean metrics. *Science* **315**, 1116–1120 (2007).

73. S. Timoshenko, Analysis of bi-metal thermostats. *J. Opt. Soc. Am.* **11**, 233 (1925).

74. M. Pezzulla, G. P. Smith, P. Nardinocchi, D. P. Holmes, Geometry and mechanics of thin growing bilayers. *Soft Matter* **12**, 4435–4442 (2016).

75. J. K. Lee, N. Stoffel, K. Fite, Electronic packaging of sensors for lower limb prosthetics, in *Proceedings of the 2012 IEEE 62nd Electronic Components and Technology Conference* (IEEE, 2012), pp. 86–91.